Monthly Notices
of the
ROYAL ASTRONOMICAL SOCIETY

MNRAS **470,** 340–349 (2017)
Advance Access publication 2017 May 15

doi:10.1093/mnras/stx1178

Constraints on the evolution of the relationship between H I mass and halo mass in the last 12 Gyr

Hamsa Padmanabhan[1]★ and Girish Kulkarni[2]

[1]*Institute for Astronomy, ETH Zurich, Wolfgang-Pauli-Strasse 27, CH-8093 Zürich, Switzerland*
[2]*Institute of Astronomy and Kavli Institute for Cosmology, University of Cambridge, Madingley Road, Cambridge CB3 0HA, UK*

Accepted 2017 May 11. Received 2017 May 11; in original form 2016 July 29

ABSTRACT

The neutral hydrogen (H I) content of dark matter haloes forms an intermediate state in the baryon cycle that connects the hot shock-heated gas and cold star-forming gas in haloes. Measurement of the relationship between H I mass and halo mass therefore puts important constraints on galaxy formation models. We combine radio observations of H I in emission at low redshift ($z \sim 0$) with optical/UV observations of H I in absorption at high redshift ($1 < z < 4$) to derive constraints on the evolution of the H I-mass–halo-mass (HIHM) relation from redshift $z = 4$ to 0. We find that one can model the HIHM relation similar to the stellar-mass–halo-mass (SHM) relation at $z \sim 0$. At $z = 0$, haloes with mass $10^{11.7}$ $M_{\odot}$ have the highest H I mass fraction (∼1 per cent), which is about four times smaller than their stellar-mass fraction. We model the evolution of the HIHM relation in a manner similar to that of the SHM relation. Combining this parametrization with a redshift- and mass-dependent modified Navarro–Frenk–White profile for the H I density within a halo, we draw constraints on the evolution of the HIHM relation from the observed H I column density, incidence rate and clustering bias at high redshift. We compare these findings with results from hydrodynamical simulations and other approaches in the literature and find the models to be consistent with each other at the 68 per cent confidence level.

Key words: galaxies: evolution – cosmology: observations – radio lines: galaxies.

1 INTRODUCTION

Understanding the evolution of neutral hydrogen (H I) in dark matter haloes is important for models of galaxy formation (Blanton & Moustakas 2009; Somerville & Davé 2015; Barkana 2016). The H I content of dark matter haloes forms an intermediate state in the baryon cycle that connects the hot shock-heated gas and star-forming molecular gas in haloes (Bouché et al. 2010; Fu et al. 2010; Krumholz & Dekel 2012). Constraints on H I in galaxies therefore reveal the role of gas dynamics, cooling and regulatory processes such as stellar feedback and gas inflow and outflow in galaxy formation (Prochaska & Wolfe 2009; van de Voort et al. 2011; Bird et al. 2015; Kauffmann et al. 2015; Bahé et al. 2016). H I also traces environmental processes like satellite quenching, tidal interactions and ram-pressure stripping (Fabello et al. 2012; Li et al. 2012; Zhang et al. 2013; Lagos et al. 2014). The average H I mass content of dark matter haloes can be expressed as an H I-mass–halo-mass (HIHM) relation.

At low redshifts ($z \sim 0$), constraints on H I in galaxies are derived from the observations of the 21-cm emission line of hydrogen in large-area blind galaxy surveys like the H I Parkes All Sky Survey (HIPASS; Meyer et al. 2004) and the Arecibo Fast Legacy ALFA survey (ALFALFA; Giovanelli et al. 2005), which provide measurements of the mass function and clustering of H I-selected galaxies. There are also targeted surveys such as The H I Nearby Galaxy Survey (THINGS; Walter et al. 2008), the *GALEX* Arecibo SDSS Survey (GASS; Catinella et al. 2010), and the Westerbork H I survey of Spiral and Irregular Galaxies (WHISP; van der Hulst, van Albada & Sancisi 2001), which focus on a smaller number of resolved galaxies. Efforts are also currently underway to constrain the density and clustering of H I using intensity mapping without resolving individual galaxies (Chang et al. 2010; Masui et al. 2013; Switzer et al. 2013). In the future, current and upcoming facilities such as MeerKAT (Jonas 2009), the Square Kilometre Array (SKA; Santos et al. 2015) and its pathfinders, and the Canadian Hydrogen Intensity Mapping Experiment (CHIME; Bandura et al. 2014) will provide unprecedented insight into the evolution of the cosmic neutral hydrogen content across redshifts.

Unfortunately, the intrinsic faintness of the 21-cm line and the limits of current radio facilities hamper direct detection of H I from individual galaxies at redshifts above $z \sim 0.1$. Spectral stacking has been used to probe the H I content of undetected sources out to redshifts $z \sim 0.24$ (Lah et al. 2007, 2009; Delhaize et al. 2013;

★ E-mail: hamsa.padmanabhan@phys.ethz.ch

Rhee et al. 2013). At higher redshifts, therefore, constraints on the distribution and evolution of H I in galaxies come chiefly from high column density Ly α absorption systems (damped Ly α absorbers; DLAs) with column density $N_{\rm H\,I} > 10^{20.2}$ cm^{-2} in the spectra of bright background sources such as quasars. DLAs are the main reservoir of H I between redshifts $z \sim 2$–5, containing >80 per cent of the cosmic H I content (Wolfe et al. 1986; Lanzetta et al. 1991; Gardner et al. 1997; Rao, Turnshek & Nestor 2006; Prochaska & Wolfe 2009; Noterdaeme et al. 2012; Zafar et al. 2013). At low redshift, DLAs have been found to be associated with galaxies (Lanzetta et al. 1991) and to contain the vast majority (∼81 per cent) of the H I gas in the local universe (Zwaan et al. 2005b). At high redshift, the kinematics of DLAs may support the hypothesis that they probe H I in large rotating discs (Prochaska & Wolfe 1997; Maller et al. 2001; Bird et al. 2015) or protogalactic clumps (Haehnelt, Steinmetz & Rauch 1998). The three-dimensional clustering of DLAs (Font-Ribera et al. 2012) points to DLAs being preferentially hosted by dark matter haloes with mass $M \sim 10^{11}\,{\rm M}_{\odot}$ at redshift $z \sim 3$.

Semi-analytical models and hydrodynamical simulations have provided clues towards the evolution of H I in galaxies and its relation to star formation, feedback and galaxy evolution (Nagamine et al. 2007; Pontzen et al. 2008; Obreschkow et al. 2009; Popping et al. 2009; Tescari et al. 2009; Hong et al. 2010; Lagos et al. 2011; Cen 2012; Duffy et al. 2012; Fu et al. 2012; Davé et al. 2013; Kim et al. 2013; Bird et al. 2014; Popping, Somerville & Trager 2014; Kim et al. 2017; Martindale et al. 2016; Crain et al. 2017). Semi-analytical methods (e.g. Berry et al. 2014; Popping, Somerville & Trager 2014; Somerville, Popping & Trager 2015) typically reproduce the H I-mass functions and the H I-to-stellar-mass scaling relations found in low-redshift H I observations and DLA observables. Simulation techniques have also been used to model DLA populations at higher redshifts (Pontzen et al. 2008) and their relation to galaxy formation and feedback processes (Rahmati et al. 2013; Bird et al. 2014; Rahmati & Schaye 2014). Hydrodynamical simulations suggest that DLAs are hosted in haloes with mass 10^{10}–$10^{11}\,h^{-1}\,{\rm M}_{\odot}$ (e.g. Bird et al. 2014). In the presence of strong stellar feedback, these simulations can reproduce the observed abundance and clustering of DLAs but end up having an excess of H I at low redshifts ($z < 3$).

Analytical techniques offer complementary insight into the processes governing the H I content of dark matter haloes. Analytical methods have been used for modelling 21-cm intensity mapping observables, particularly the H I bias and power spectrum (Marín et al. 2010; Wyithe & Brown 2010; Sarkar, Bharadwaj & Anathpindika 2016) as well as DLAs (Haehnelt, Rauch & Steinmetz 1996; Haehnelt, Steinmetz & Rauch 1998; Barnes & Haehnelt 2009, 2010; Kulkarni et al. 2013; Barnes & Haehnelt 2014). These models use prescriptions for assigning H I mass to dark matter haloes as inputs to the model, either directly or in conjunction with cosmological simulations (Bagla, Khandai & Datta 2010; Marín et al. 2010; Gong et al. 2011; Guha Sarkar et al. 2012). In Padmanabhan, Choudhury & Refregier (2016), the 21-cm and DLA-based analytical approaches are combined towards a consistent model of H I evolution across redshifts. It is found that a model that is consistent with low-redshift radio as well as high-redshift optical/UV observations requires a fairly rapid transition of H I from low-mass to higher mass haloes at high redshifts. A more complete statistical data-driven approach (Padmanabhan & Refregier 2017) constrains the HIHM relation using low- and high-redshift observations in a halo model framework.

An essential ingredient in analytical techniques is therefore the HIHM relation. In this paper, we employ the technique of abundance matching to quantify the observational constraints on the HIHM relation in the post-reionization Universe. Abundance matching has been widely used to describe the relation between the stellar mass of galaxies and the mass of their host dark matter haloes (Vale & Ostriker 2004, 2006; Conroy, Wechsler & Kravtsov 2006; Shankar et al. 2006; Behroozi, Conroy & Wechsler 2010; Guo et al. 2010; Moster et al. 2010; Moster, Naab & White 2013). The basic assumption involved is that there is a monotonic relationship between a galaxy property (say, stellar mass or galaxy luminosity) and the host dark matter halo property (say, the host halo mass). In its simplest form, abundance matching involves matching the cumulative abundance of galaxies to that of their (sub)haloes, thereby assigning the most luminous galaxies to the most massive haloes. The mapping between the underlying galaxy property and the host halo mass can be derived from this. A key feature of this approach is that being completely empirical,[1] it is free from the uncertainties involved in physical models of H I and galaxy evolution. It is therefore a complementary analysis to forward modelling techniques, including semi-analytical models and hydrodynamical simulations.

The H I-mass function (Rao & Briggs 1993) is the radio equivalent of the optical luminosity function in galaxies and is an important statistical quantity in the observations of gas-rich galaxies. It measures the volume density of H I-selected galaxies as a function of the H I mass, and simulations suggest that its shape is a more sensitive probe of some aspects of galaxy formation physics than the galaxy luminosity function (Kim et al. 2013). At low redshifts, the H I-mass function is fairly well constrained over four decades in H I mass (Zwaan et al. 2005a; Martin et al. 2010). Papastergis et al. (2013) constrained the HIHM relation at low redshift using ALFALFA data and found that the observed clustering of H I was reproduced well by this approach. In this work, we describe the results of abundance matching H I mass to dark matter halo mass using the low-redshift radio observations of the H I-mass function (Zwaan et al. 2005a; Martin et al. 2010) and then evolve the relation using the complementary information available through DLA measurements at high redshift. The combination of the radio data at low redshifts and DLA observations at higher redshifts constrains a multi-epoch H I mass–halo mass relation with the available data. We also compare how the results from this approach are consistent with those from studies in previous literature.

The paper is organized as follows. In Section 2, we detail the abundance matching technique and apply it to three low-redshift H I-mass function measurements. We also combine the resultant HIHM relation with the stellar-mass–halo-mass (SHM) relation to discuss the H I-to-stellar-mass ratio in low-redshift galaxies. In Section 3, we extend the low-redshift HIHM relation to higher redshifts using measurements of DLA column density distribution and clustering. We compare the relation so derived with other H I models in the literature and conclude in Section 4.

2 HIHM RELATION AT LOW REDSHIFT

We derive the HIHM relation at $z \sim 0$ by abundance matching dark matter haloes with H I-selected galaxies. We use the H I-mass function from the HIPASS (Meyer et al. 2004) and ALFALFA (Martin et al. 2010) data sets, the latter derived using the $1/V_{\rm max}$ as well as the 2-Dimensional StepWise Maximum Likelihood (2DSWML) methods, which are as follows:

[1] A caveat is that the halo-mass function being used is theoretical, and the assumption of matching the most massive haloes is involved.

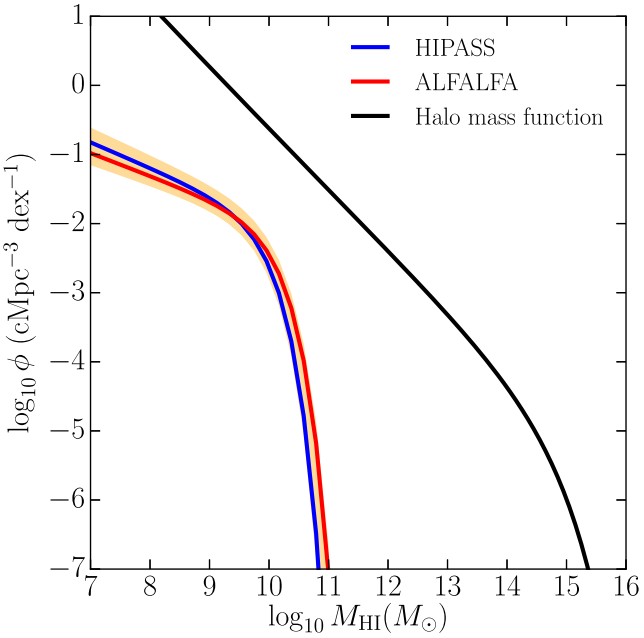

Figure 1. The blue and red curves show the H I-mass functions derived from the HIPASS (Zwaan et al. 2005a) and ALFALFA data (Martin et al. 2010), respectively. The shaded region shows the combined uncertainty. The black curve shows the halo-mass function.

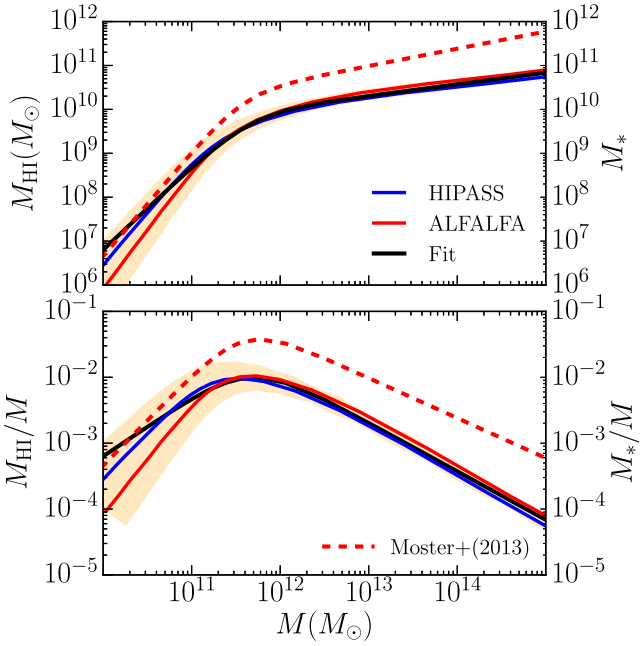

Figure 2. Top panel: the HIHM relation at $z = 0$ derived from HIPASS (blue curve) and ALFALFA (red curve) H I-mass functions. The black curve shows a combined fit to the mass functions using the parametric form of equation (2). The shaded region shows the error in the fit. Lower panel: the H I mass fraction $M_{\rm H\,I}/M$ as a function of halo mass M at $z = 0$. Also shown for comparison in both panels is the SHM relation (Moster et al. 2013).

(i) HIPASS: this complete catalogue of H I sources contains 4315 galaxies (Meyer et al. 2004). The H I-mass function $\phi(M_{\rm H\,I})$ is fitted by a Schechter function using the 2DSWML method, with a total of 4010 galaxies. The effective volume $V_{\rm eff}$ is calculated for each galaxy individually and the values of $1/V_{\rm eff}$ are summed in bins of H I mass to obtain the 2DSWML mass function. The resultant best-fitting parameters are $\alpha = -1.37 \pm 0.03 \pm 0.05$, $\log(M_*/{\rm M}_\odot) = 9.80 \pm 0.03 \pm 0.03\ h_{75}^{-2}$ and $\phi^* = (6.0 \pm 0.8 \pm 0.6) \times 10^{-3}\ h_{75}^3$ Mpc^{-3} (the two error values show statistical and systematic errors, respectively; Zwaan et al. 2005a). The distribution of H I masses is calculated using 30 equal-sized mass bins spanning $6.4 < \log_{10} M_{\rm H\,I} < 10.8$ (in $\rm M_\odot$).

(ii) ALFALFA: this catalogue contains 10 119 sources to form the largest available sample of H I-selected galaxies (Martin et al. 2010). The ALFALFA survey measures the H I-mass function by using both the 2DSWML and the $1/V_{\rm max}$ methods. The H I-mass function is fitted with the Schechter form, with the best-fitting parameters $\phi^* = (4.8 \pm 0.3) \times 10^{-3}\ h_{70}^3$ Mpc^{-3}, $\log(M_*/{\rm M}_\odot) + 2\log(h_{70}) = 9.95 \pm 0.04$, and $\alpha = -1.33 \pm 0.03$ with the $1/V_{\rm max}$ method, and $\phi^* = (4.8 \pm 0.3) \times 10^{-3}\ h_{70}^3$ Mpc^{-3}, $\log(M_*/{\rm M}_\odot) + 2\log(h_{70}) = 9.96 \pm 0.2$, and $\alpha = -1.33 \pm 0.02$ with the 2DSWML method. The two determinations of the H I-mass function are in good agreement.[2]

To match H I-selected galaxies to dark matter haloes, we use the Sheth–Tormen (Sheth & Tormen 2002) form of the dark matter halo-mass function. Fig. 1 shows the comparison of the three H I-mass functions mentioned above with the halo-mass function, which is shown by the solid black curve. This corresponds to the assumption that each dark matter halo hosts one H I galaxy with its H I mass proportional to the host dark matter halo mass. The shaded region in Fig. 1 shows the combined uncertainty in the observed H I-mass functions. Matching the abundance of the halo-mass function and the fitted H I-mass function then leads to the relation between the H I mass and the halo mass (e.g. Vale & Ostriker 2004):

$$\int_{M(M_{\rm H\,I})}^{\infty} \frac{{\rm d}n}{{\rm d}\log_{10} M'}\,{\rm d}\log_{10} M' = \int_{M_{\rm H\,I}}^{\infty} \phi(M'_{\rm H\,I})\,{\rm d}\log_{10} M'_{\rm H\,I}, \qquad (1)$$

where ${\rm d}n/{\rm d}\log_{10}M$ is the number density of dark matter haloes with logarithmic masses between $\log_{10}M$ and $\log_{10}(M + {\rm d}M)$, and $\phi(M_{\rm H\,I})$ is the corresponding number density of H I galaxies in logarithmic mass bins. Solving equation (1) gives a relation between the H I-mass $M_{\rm H\,I}$ and the halo-mass M. Note that this approach assumes that there is a monotonic relationship between $M_{\rm H\,I}$ and M.

Solving equation (1) in the mass range of $10^6\ {\rm M}_\odot < M_{\rm H\,I} < 10^{11}\ {\rm M}_\odot$, we show the resultant HIHM relation in the top panel of Fig. 2. The red curve shows the HIHM relation obtained from the ALFALFA data, while the blue curve shows the same for the HIPASS data. We find that the H I mass monotonically increases as a function of the halo mass and changes slope at a characteristic value of the halo mass. This behaviour is qualitatively similar to the SHM relation (Moster et al. 2013), which is shown by the dashed red curve in the top panel of Fig. 2. For small mass haloes, the H I mass is nearly equal to the stellar mass. But the H I mass decreases more rapidly than the stellar mass as a function of halo mass, and for high-mass haloes the H I mass is down to almost a tenth of the stellar mass. The characteristic mass for the HIHM relation is also slightly smaller ($10^{11.7}\ {\rm M}_\odot$) than that for the SHM relation ($\sim 10^{12}\ {\rm M}_\odot$). The HIHM relation is shown as the ratio of the H I and halo masses in the lower panel of Fig. 2. The peak H I mass fraction is about 1 per cent, and this reduces down to 0.01 per cent at both high and low masses. The peak H I mass fraction is in good agreement with the abundance matching estimates of Rodríguez-Puebla et al. (2011), Evoli et al. (2011) and Baldry, Glazebrook & Driver (2008) and the direct estimate of Papastergis et al. (2012) for

[2] In the figures, we only indicate the ALFALFA 2DSWML mass function fit for clarity.

the baryonic mass fraction. It had been found that the clustering of the H I-selected galaxies in ALFALFA (Papastergis et al. 2013) was also well matched by abundance matching at $z \sim 0$, and the cold gas fraction showed a maximum at halo masses close to $10^{11.1-11.3}$ $M_\odot$, which was lower than the corresponding peak for the stellar-mass fraction ($10^{11.8}$ $M_\odot$).

We parametrize the HIHM relation by a function of the form introduced for the SHM relation by Moster et al. (2013),

$$M_{\rm H\,I} = 2N_{10}M\left[\left(\frac{M}{M_{10}}\right)^{-b_{10}} + \left(\frac{M}{M_{10}}\right)^{y_{10}}\right]^{-1}. \quad (2)$$

We fit the HIHM relation by the function of this form using non-linear least squares. The best-fitting values of the free parameters are $M_{10} = (4.58 \pm 0.19) \times 10^{11}$ $M_\odot$, $N_{10} = (9.89 \pm 4.89) \times 10^{-3}$, $b_{10} = 0.90 \pm 0.39$ and $y_{10} = 0.74 \pm 0.03$. The errors here are estimated by propagating the uncertainties in Fig. 1. The best-fitting HIHM relations are shown in Fig. 2 (black curves), with the corresponding error indicated by the shaded region.

2.1 The H I-mass–stellar-mass relation

We can combine our derived HIHM relation with known SHM relations to understand the relationship between the H I mass and stellar mass in dark matter haloes. Moster et al. (2013) use a multi-epoch abundance matching method with observed stellar-mass functions (SMFs) to describe the evolution of the SHM relation across redshifts. At each redshift, they parametrize the SHM relation using the functional form in equation (2). At low redshifts, the SMFs of Li & White (2009) based on the Sloan Digital Sky Survey (SDSS) DR7 (York et al. 2000; Abazajian et al. 2009) are used, along with the observations of Baldry et al. (2008). At higher redshifts, the SMFs by Pérez-González et al. (2008) are used for massive galaxies and those by Santini et al. (2012) for the low-mass galaxies. From the results of abundance matching, the mean SHM relation is obtained, which is then used to populate haloes in the Millennium (MS-I; Springel et al. 2005) and the Millennium-II (MS-II; Boylan-Kolchin et al. 2009) simulations with galaxies. From this, the model SMFs are derived and directly compared to observations to constrain the free parameters in the SHM relation. The resulting mean stellar-mass fraction at $z \sim 0$ is shown by the dashed line in Fig. 2.

We use the Moster et al. (2013) results for the SHM relation, coupled to our abundance matching results for HIHM to arrive at an H I-mass–stellar-mass relation. This is shown by the solid red and blue curves in Fig. 3 for HIPASS and ALFALFA, respectively. The 68 per cent scatter in the relation is indicated by the blue band. For comparison, we also show the measurements from 750 galaxies in the redshift range $0.025 < z < 0.05$ and $M_* > 10^{10}$ $M_\odot$ from the GASS (Catinella et al. 2010, 2013), and 366 galaxies from the COLD GASS survey (Saintonge et al. 2011a,b; Catinella et al. 2012). We also show results from Leroy et al. (2008), which is a compilation of individual galaxies detected in the HERA CO Line Extragalactic Survey (HERACLES; Leroy et al. 2009) that are part of THINGS (Walter et al. 2008), which covers H I masses in the range of (0.01–14) $\times$ 10^9 $M_\odot$. These measurements are consistent with our result, although the observational data exhibit a somewhat large scatter. We note that the H I-mass –stellar-mass relation from the ALFALFA data and the THINGS data show some discrepancy at low stellar masses (also seen in Popping, Behroozi & Peeples 2015, which matches the data in Leroy et al. 2008, but has difficulty matching the ALFALFA data mass function at low H I masses).

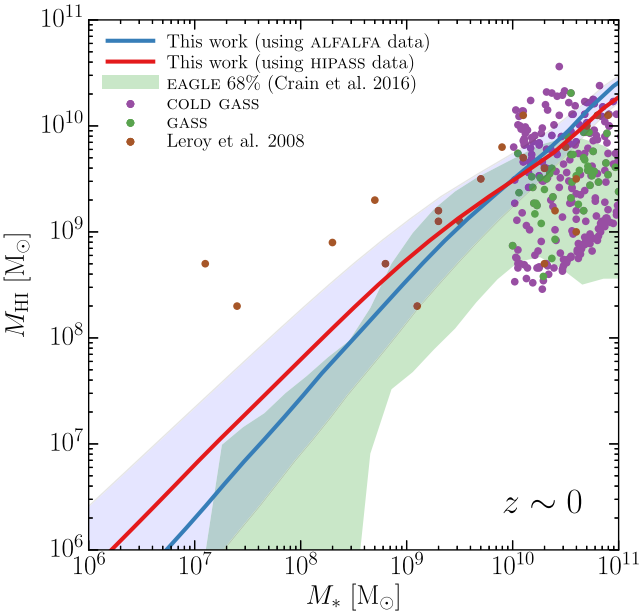

Figure 3. The H I-mass–stellar-mass relation obtained by abundance matching combined with the SHM relation determined by Moster et al. (2013) are shown by the solid curves. The 68 per cent scatter in the relation is indicated by the blue band. The green band shows the region around the median in which 68 per cent of the galaxies in the EAGLE reference simulation lie on this plane (Crain et al. 2017). Also shown are the data from individual objects detected in the GASS and COLD GASS surveys, and the nearby galaxies in HERACLES and THINGS (Leroy et al. 2008).

However, the main aim of this work is to provide an understanding of the HIHM relation, and as such, we do not conjecture on the observed discrepancy of the Leroy et al. (2008) results with the ALFALFA data. We also compare our H I-mass–stellar-mass relation with that found in the EAGLE hydrodynamical simulations (Crain et al. 2015; Schaye et al. 2015). The EAGLE simulations model the formation and evolution of galaxies in the presence of various feedback processes. They also model the H I content of galaxies by using calibrated fitting functions from radiative transfer simulations to estimate self-shielding, and also employing empirical relations to correct for molecular gas formation (Crain et al. 2017). The green band in Fig. 3 shows the region around the median on the H I-mass stellar-mass diagram occupied by 68 per cent of galaxies in the reference EAGLE simulation (labelled 'L100N1504' in Schaye et al. 2015). Our results are in good agreement with the EAGLE predictions, except possibly at the highest stellar masses ($M_* > 10^{10}$ $M_\odot$), where the H I mass in EAGLE galaxies starts to decrease. This is likely a reflection of the AGN feedback in EAGLE that heats and expunges cold gas from high-mass galaxies by their massive central black holes (Crain et al. 2017).

Fig. 4 shows the H I-mass-to-stellar-mass ratio as a function of the halo mass. The blue and red curves show the results for HIPASS and ALFALFA, respectively, and the black curve shows the parametrized fit. In each case, we obtain the H I-mass-to-stellar-mass ratio by combining our HIHM relation with the SHM relation of Moster et al. (2013). The H I-mass-to-stellar-mass ratio is about 25 per cent in a rather broad range of halo masses from 10^{11} to 10^{13} $M_\odot$. The ratio decreases to about 10 per cent at halo masses above this range, and is more uncertain below this range, due to the uncertainty in the data and the fitting (Fig. 2 lower panel) at lower masses. The shaded regions show the uncertainty in the

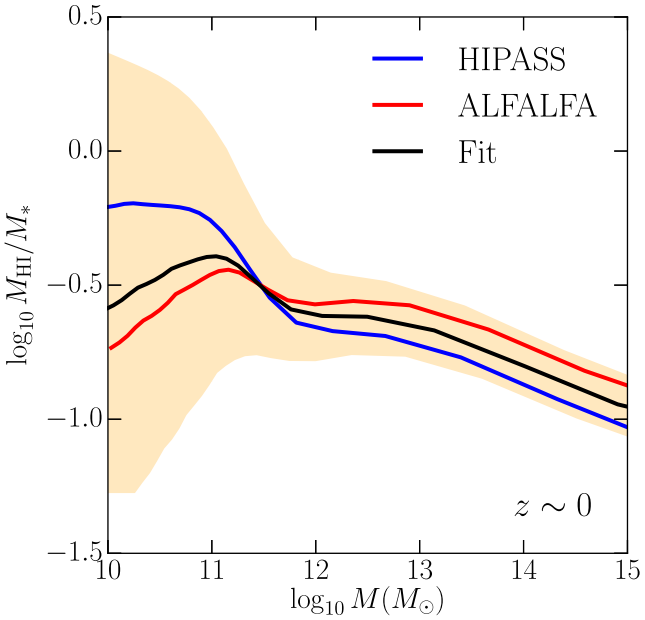

Figure 4. The H I-mass to stellar-mass ratio as a function of the halo mass at $z \sim 0$. The blue and red curves combine our results for HIPASS and ALFALFA data, respectively, with the SHM relation from Moster et al. (2013). The parametrized fit is indicated by the black curve. The shaded region shows the uncertainty in the H I-mass to stellar-mass ratio obtained by propagating errors from Fig. 2.

H I-mass-to-stellar-mass ratio, obtained by propagating the errors from Fig. 2.

3 HIHM RELATION AT HIGH REDSHIFT

Due to the intrinsic faintness of the 21-cm line, the direct detection of H I from resolved galaxies is difficult at redshifts above $z \sim 0.1$. At higher redshifts ($z < 5$), therefore, constraints on the distribution and evolution of H I in galaxies mainly come from high column density Ly α absorption systems (DLAs) with column densities $N_{\rm H\,I} > 10^{20.3}$ cm^{-2} in the spectra of bright background sources such as quasars. The relevant observables at these redshifts are the incidence rate $\mathrm{d}N/\mathrm{d}X$ of DLAs, the column density distribution $f_{\rm H\,I}(N_{\rm H\,I}, z)$ of DLAs at high column densities, the three-dimensional clustering of DLAs as quantified by their clustering bias relative to the underlying dark matter, and the total amount of neutral hydrogen in DLAs (Wolfe et al. 1986; Lanzetta et al. 1991; Gardner et al. 1997; Rao et al. 2006; Prochaska & Wolfe 2009; Noterdaeme et al. 2012; Zafar et al. 2013). A detailed summary of the low- and high-redshift H I observables is provided in Padmanabhan, Choudhury & Refregier (2015). We now extend the HIHM relation obtained at $z = 0$ to higher redshifts by using these observables. Throughout the analysis, we use the cosmological parameters $h = 0.71$, $\Omega_{\rm m} = 0.281$, $\Omega_\Lambda = 0.719$, $\sigma_8 = 0.8$, $n_{\rm s} = 0.964$.

3.1 Modelling the H I observables

To model the distribution of H I density within individual dark matter haloes, we use the redshift- and mass-dependent modified Navarro–Frenk–White (NFW; Navarro, Frenk & White 1996) profile introduced by Barnes & Haehnelt (2014):

$$\rho_{\rm H\,I}(r) = \frac{\rho_0 r_{\rm s}^3}{(r + 0.75 r_{\rm s})(r + r_{\rm s})^2}, \tag{3}$$

where $r_{\rm s}$ is the scale radius defined as $r_{\rm s} = R_{\rm v}(M)/c(M, z)$, with $R_{\rm v}(M)$ being the virial radius of the halo. The halo concentration parameter $c(M, z)$ is approximated by

$$c(M, z) = c_{\rm H\,I} \left(\frac{M}{10^{11}\,{\rm M}_\odot}\right)^{-0.109} \left(\frac{4}{1+z}\right). \tag{4}$$

The profile in equation (3) is motivated by the analytical modelling of cooling in multiphase halo gas by Maller & Bullock (2004). In the above equation, $c_{\rm H\,I}$ is a free parameter, the concentration parameter for the H I, analogous to the dark matter halo concentration $c_0 = 3.4$ (Macciò et al. 2007). The value of this parameter can be constrained by fitting to the observations. The ρ_0 in equation (3) is determined by normalization to the total H I mass:

$$\int_0^{R_{\rm v}(M)} 4\pi r^2 \rho_{\rm H\,I}(r)\mathrm{d}r = M_{\rm H\,I}(M). \tag{5}$$

Thus, both the H I–halo–mass relation and the radial distribution of H I are required for constraining the H I profile.

The DLA-based quantities at different redshifts can now be computed by defining the column density of a halo at impact parameter s as (Barnes & Haehnelt 2014; Padmanabhan et al. 2016)

$$N_{\rm H\,I}(s) = \frac{2}{m_H} \int_0^{\sqrt{R_{\rm v}(M)^2 - s^2}} \mathrm{d}l\ \rho_{\rm H\,I}\left(\sqrt{s^2 + l^2}\right), \tag{6}$$

where $m_{\rm H}$ is the hydrogen atom mass and $R_{\rm v}(M)$ is the virial radius associated with a dark matter halo of mass M. We define the DLA cross-section of the halo as $\sigma_{\rm DLA} = \pi s_*^2$, where s_* is defined such that $N_{\rm H\,I}(s_*) = 10^{20.3}$ cm^{-2}. The clustering bias of DLAs, $b_{\rm DLA}$, can then be written as

$$b_{\rm DLA}(z) = \frac{\int_0^\infty \mathrm{d}M n(M, z) b(M, z) \sigma_{\rm DLA}(M, z)}{\int_0^\infty \mathrm{d}M n(M, z) \sigma_{\rm DLA}(M, z)}, \tag{7}$$

where $n(M, z)$ is the comoving halo-mass function and $b(M, z)$ is the clustering bias factor of haloes (Scoccimarro et al. 2001). The DLA incidence $\mathrm{d}N/\mathrm{d}X$ can be calculated as

$$\frac{\mathrm{d}N}{\mathrm{d}X} = \frac{c}{H_0} \int_0^\infty n(M, z) \sigma_{\rm DLA}(M, z)\, \mathrm{d}M, \tag{8}$$

and the column density distribution $f_{\rm H\,I}(N_{\rm H\,I}, z)$ is given by

$$f(N_{\rm H\,I}, z) \equiv \frac{\mathrm{d}^2 n}{\mathrm{d}X \mathrm{d}N_{\rm H\,I}} = \frac{c}{H_0} \int_0^\infty n(M, z) \left|\frac{\mathrm{d}\sigma}{\mathrm{d}N_{\rm H\,I}}(M, z)\right| \mathrm{d}M, \tag{9}$$

where

$$\frac{\mathrm{d}\sigma}{\mathrm{d}N_{\rm H\,I}} = 2\pi s \frac{\mathrm{d}s}{\mathrm{d}N_{\rm H\,I}}, \tag{10}$$

with $N_{\rm H\,I}(s)$ defined by equation (6). The density parameter for DLAs, $\Omega_{\rm DLA}$, is obtained by integrating the column density distribution:

$$\Omega_{\rm DLA}(N_{\rm H\,I}, z) = \frac{m_{\rm H} H_0}{c \rho_{\rm c,0}} \int_{10^{20.3}}^\infty f_{\rm H\,I}(N_{\rm H\,I}, z)\, N_{\rm H\,I}\, \mathrm{d}N_{\rm H\,I}, \tag{11}$$

where $\rho_{\rm c,0}$ is the present-day critical density.

At high redshifts, we also use the measurement of $\Omega_{\rm H\,I} b_{\rm H\,I}$ from H I intensity mapping at $z \sim 0.8$ by Switzer et al. (2013). To calculate this quantity in our model, the H I density parameter is given by

$$\Omega_{\rm H\,I}(z) = \frac{1}{\rho_{\rm c,0}} \int_0^\infty n(M, z) M_{\rm H\,I}(M, z) \mathrm{d}M\,. \tag{12}$$

The bias of H I is given by

$$b_{\rm H\,I}(z) = \frac{\int_0^\infty {\rm d}M n(M,z) b(M,z) M_{\rm H\,I}(M,z)}{\int_0^\infty {\rm d}M n(M,z) M_{\rm H\,I}(M,z)}, \quad (13)$$

where $b(M, z)$ is the dark matter halo bias. We fit the H I density profiles of haloes at $z = 0$ by using the column density distribution at $z = 0$ for $N_{\rm H\,I} > 10^{20.3}$ cm^{-2}, derived from the WHISP data by Zwaan et al. (2005b).

3.2 Extending the HIHM relation to high redshifts

We can now extend the HIHM relation developed in Section 2 to higher redshifts. We do this by parametrizing the HIHM relation evolution in a manner similar to the parametrization of the SHM relation evolution by Moster et al. (2013). We write the HIHM relation at higher redshifts as

$$M_{\rm H\,I} = 2N_1 M \left[\left(\frac{M}{M_1} \right)^{-b_1} + \left(\frac{M}{M_1} \right)^{y_1} \right]^{-1}, \quad (14)$$

which has the same form as equation (2). The parameters in equation (14) are written as

$$\begin{aligned} \log_{10} M_1 &= \log_{10} M_{10} + \frac{z}{z+1} M_{11}, \\ N_1 &= N_{10} + \frac{z}{z+1} N_{11}, \\ b_1 &= b_{10} + \frac{z}{z+1} b_{11}, \text{ and} \\ y_1 &= y_{10} + \frac{z}{z+1} y_{11}. \end{aligned} \quad (15)$$

The parameters M_{10}, N_{10}, b_{10} and y_{10} are defined in equation (2) for $z = 0$. The four additional parameters, M_{11}, N_{11}, b_{11} and y_{11}, introduced by equations (15) govern the evolution of the HIHM at high redshift. These four parameters together with the H I density profile parameter $c_{\rm H\,I}$ are to be constrained from the high-redshift observations. This is done by using the data available from $z = 0$ to 5 as summarized in Table 1. We use the measurements of the incidence rate ${\rm d}N/{\rm d}X$ of DLAs, the column density distribution $f_{\rm H\,I}(N_{\rm H\,I}, z)$ of DLAs at high column densities, the three-dimensional clustering of DLAs as quantified by their clustering bias relative to the dark matter and the total amount of neutral hydrogen in DLAs (Wolfe et al. 1986; Lanzetta et al. 1991; Gardner et al. 1997; Rao et al. 2006; Prochaska & Wolfe 2009; Noterdaeme et al. 2012; Zafar et al. 2013), as well as the measurements of the H I column density distribution and clustering from radio data at $z < 1$ (Zwaan et al. 2005b; Switzer et al. 2013).

Table 1. High-redshift data used in this paper. The measurement of $\Omega_{\rm H\,I} b_{\rm H\,I}$ comes from H I intensity mapping at $z \sim 0.8$ by Switzer et al. (2013). Rao et al. (2006) use measurements of absorption systems at median redshifts $z \sim 0.609$ and $\sim$1.219 to derive the DLA parameters. All other data come from Ly α absorption measurements using high-redshift quasar spectra.

z	Observable	Source
$\sim$1	$\Omega_{\rm H\,I} b_{\rm H\,I}$	Switzer et al. (2013)
	$f_{\rm H\,I}$	Rao et al. (2006)
	${\rm d}N/{\rm d}X$	Rao et al. (2006)
2.3	$\Omega_{\rm DLA}$	Zafar et al. (2013)
	$f_{\rm H\,I}$	Noterdaeme et al. (2012)
	$b_{\rm DLA}$	Font-Ribera et al. (2012)
	${\rm d}N/{\rm d}X$	Zafar et al. (2013)
> 3	${\rm d}N/{\rm d}X$	Zafar et al. (2013)

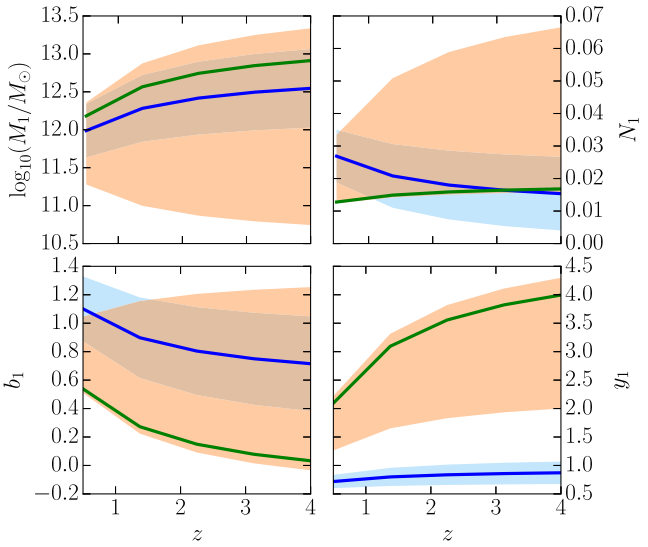

Figure 5. The evolution of the parameters of the HIHM relation (equation 14). The green curves show our best-fitting parameter inferences with 68 per cent confidence intervals shown by the orange shaded region. For comparison, the evolution of the corresponding quantities for the SHM relation of Moster et al. (2013) is shown in blue.

The best-fitting values for the five parameters M_{11}, N_{11}, b_{11}, y_{11} and $c_{\rm H\,I}$, and their errors are now estimated by a Bayesian Markov Chain Monte Carlo (MCMC) analysis using the COSMOHAMMER package (Akeret et al. 2013). The likelihood

$$\mathcal{L} = \exp\left(-\frac{\chi^2}{2}\right) \quad (16)$$

is maximized with respect to the five free parameters, with

$$\chi^2 = \sum_i \frac{(f_{\rm i} - f_{\rm obs,i})^2}{\sigma^2_{\rm obs,i}}, \quad (17)$$

where the $f_{\rm i}$ are the model predictions, $f_{\rm obs,i}$ are the observational data and $\sigma^2_{\rm obs,i}$ are the squares of the associated uncertainties (here assumed independent).

The best-fitting parameters and their 68 per cent errors are $M_{11} = 1.56^{+0.53}_{-2.70}$, $N_{11} = 0.009^{+0.06}_{-0.001}$, $b_{11} = -1.08^{+1.52}_{-0.08}$, $y_{11} = 4.07^{+0.39}_{-2.49}$, and $c_{\rm H\,I} = 133.66^{+81.39}_{-56.23}$. The inferred evolution of the four parameters of the HIHM relation in equation (14) is shown in Fig. 5 together with the 68 per cent errors. For comparison, the evolution of the corresponding parameters in the SHM relation parametrization of Moster et al. (2013) are also shown. The model allows for a wide range of parameters in the HIHM relation at high redshifts. The increase in the best-fitting characteristic mass follows the increase in the characteristic halo mass of the SHM relation. The evolution of the high-mass slope y_1 is much more rapid for the HIHM relation than the SHM relation. As we will see below, the high value of the clustering bias factor for DLAs at high redshifts forces the increase in the characteristic halo mass of the HIHM relation, but the more gradual increase observed in the DLA incidence rate prevents us from putting too much H I in high-mass haloes, which constrains the high-mass slope to very steep values.

Fig. 6 shows the column density distribution derived from our model at $z \sim 0$, 1 and 2.3 together with the associated 68 per cent statistical error.

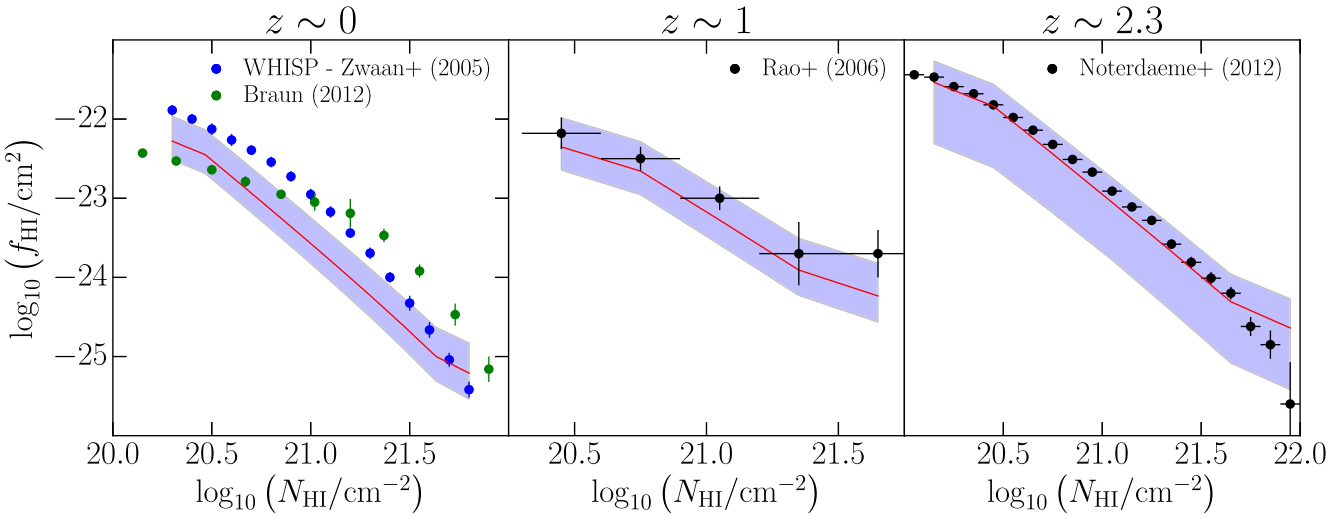

Figure 6. The best-fitting column density distribution (red curves) in our model at redshifts 0, 1 and 2.3, compared to the observations. The blue shaded regions show the 68 per cent confidence limits. The model fits the high-redshift column density distributions quite well but has difficulty in fitting the column density distribution at $z = 0$, especially at low column densities.

At $z \sim 0$, only the concentration parameter of the profile is used to obtain the column density distribution, since the HIHM relation has been directly fixed by the results of abundance matching. The concentration parameter is assumed to be equal to that obtained from the fitting of higher redshifts, which is done using the analysis outlined in Section 3.2. The relation fits the available data reasonably well, but leads to an underprediction of the observed column density distribution at $z \sim 0$ at low column densities ($N_{\rm H\,I} < 10^{21.4}$ cm^{-2}).[3] Fig. 7 compares other quantities in our model to their observed values. The incidence rate of DLAs is fit very well by the model throughout the redshift range considered here. The measurements of the density parameters of H I and DLAs, and the clustering bias of $z \sim 2.3$ DLAs are also fit well. The fit to the measured H I bias at $z = 0$ is also good, although it is somewhat poor at $z = 1$.

3.3 Comparison to other models of H I at high redshift

Fig. 8 shows the inferred best-fitting HIHM at $z = 0$, 1, 2, 3 and 4 in the present model, together with their associated uncertainties. In each case, the black curve shows the best-fitting HIHM relation and the grey band shows the 68 per cent scatter around it. The figure also presents a comparison of the HIHM obtained from hydrodynamical simulations and other approaches in the literature at $z = 0$, 1, 2 and 3. These are briefly described below:

(i) At $z = 0$, the model that comes closest to this work is the non-parametric HIHM relation of Marín et al. (2010), although their low-mass slope is shallower.

[3] The two data sets for the column density distribution at $z \sim 0$ (which indicate a systematic offset) are shown only for comparison, and not directly fitted. The parameters involved in the HIHM are obtained from the abundance matching fits, and the concentration parameter is obtained from the results of the higher redshift column density fitting. The steep slope of the HIHM relation for $z = 0$ leads to a lower column density distribution than observed, suggesting that the altered NFW profile may not fully describe the H I density profiles of haloes at $z = 0$, or that there may be a possible tension between the H I-mass function and the column density distribution at $z = 0$. We will explore this issue in further detail in future work.

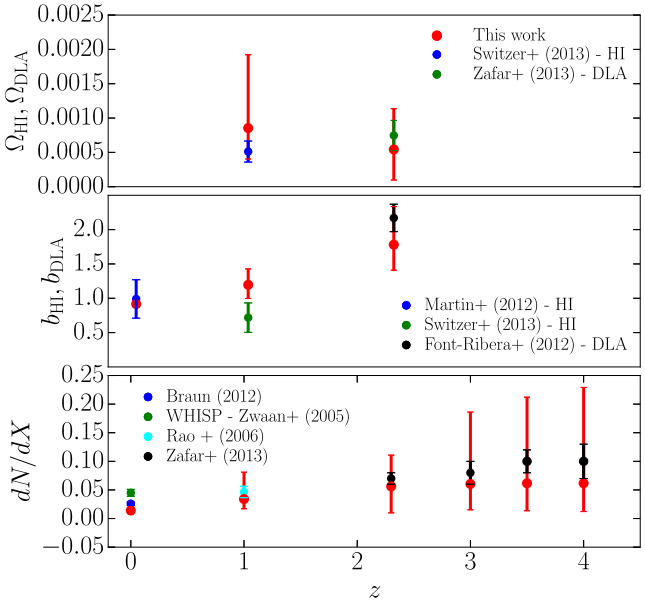

Figure 7. Our model predictions for the density parameter, clustering bias and DLA incidence rate (red, with 68 per cent confidence intervals indicated by the error bars) compared to the observations. Note that at redshift $z \sim 1$, Switzer et al. (2013) constrain the product $\Omega_{\rm H\,I} b_{\rm H\,I}$. Shown here is the observed $\Omega_{\rm H\,I} b_{\rm H\,I}$ divided by the model value of $b_{\rm H\,I}$ (top panel) and $\Omega_{\rm H\,I}$ (second panel). The model successfully matches these observations, including the bias at high redshifts.

(ii) The hydrodynamical simulations of Davé et al. (2013) produce an HIHM relation that has very similar high-mass and low-mass slopes as the present HIHM relation. The high characteristic mass of the average best-fitting HIHM relation in this work is a natural consequence of matching the abundance of haloes with H I-selected galaxies, under the assumption that H I-mass of dark matter haloes scales monotonically with their virial mass.

(iii) Bagla et al. (2010) used a set of analytical prescriptions to populate H I in dark matter haloes. In their simplest model, H I was assigned to dark matter haloes with a constant fraction f by mass, within a mass range. The maximum and minimum masses of

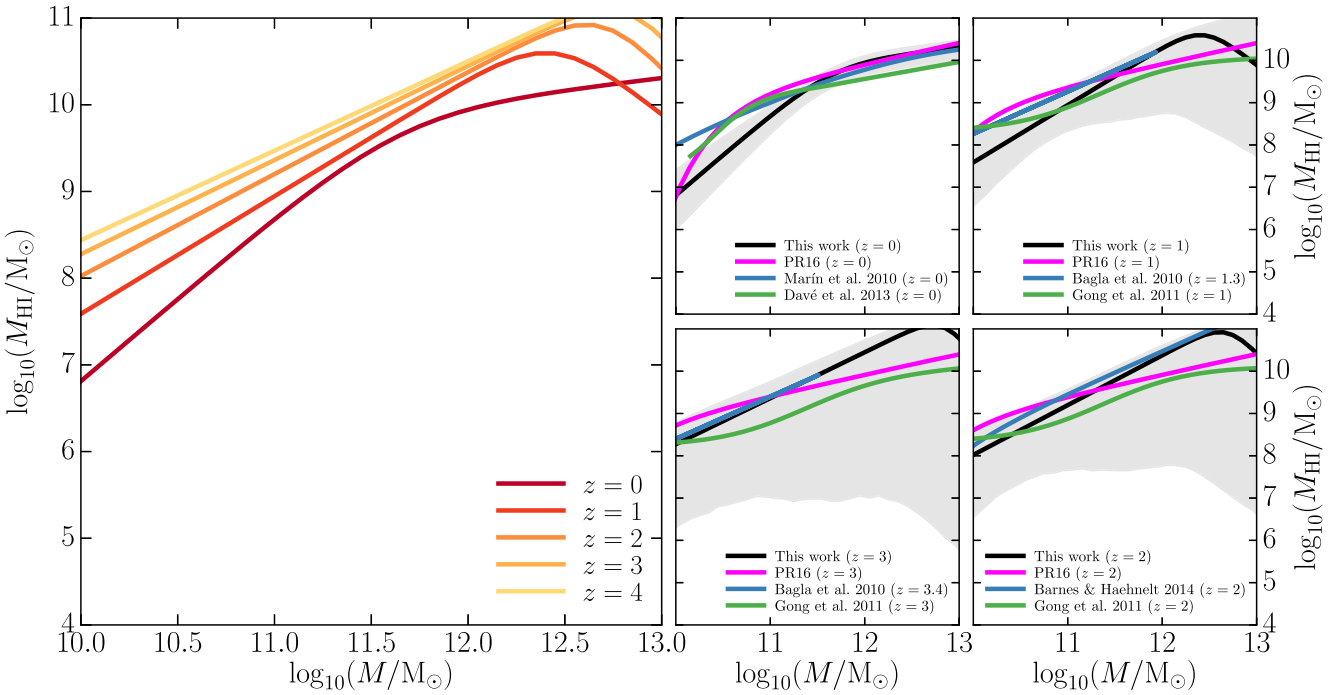

Figure 8. Left-hand panel: the HIHM relation inferred at redshifts $z = 0$, 1, 2, 3 and 4 from this work. Right-hand panels: the HIHM relation in this work compared to the results of other approaches in the literature at redshifts $z = 0$, 1, 2 and 3.

haloes that host H I were assumed to be redshift-dependent. It was also assumed that haloes with virial velocities of greater than 200 km s^{-1} and less than 30 km s^{-1} do not host any H I.

(iv) Gong et al. (2011) provide non-linear analytical forms of the HIHM relation at $z = 1$, 2 and 3, derived from the results of the simulations of Obreschkow et al. (2009). These predict a slightly different form for the HIHM relation.

(v) The model of Barnes & Haehnelt (2014) uses an HIHM relation that reproduces the observed bias of DLA systems at $z \sim 2.3$ and constrains stellar feedback in shallow potential wells.

(vi) Padmanabhan & Refregier (2017) used a statistical data-driven approach to derive the best-fitting HIHM relation and radial distribution profile $\rho_{\rm H\,I}(r)$ for $z = 0$–4, from a joint analysis combining the data from the radio observations at low redshifts and the DLA system observables at high redshifts, along the lines of this work. This approach also produces results consistent with this work, although the present best-fitting HIHM relation at high redshifts may prefer a higher characteristic halo mass.

It can be seen that all these models are consistent with each other and with the data at the 68 per cent confidence level. Tighter constraints on the HIHM relation at high redshifts may be achieved with the availability of better quality data with upcoming radio telescopes.

4 CONCLUSIONS

In this paper, we have explored the evolution of the neutral hydrogen content of galaxies in the last 12 Gyr (redshifts $z = 0$–4). At redshift $z = 0$, this work follows the approach of abundance matching, which has been widely used for the stellar mass content of galaxies to model galaxy luminosity functions (Vale & Ostriker 2004, 2006; Conroy et al. 2006; Shankar et al. 2006; Behroozi et al. 2010; Guo et al. 2010; Moster et al. 2010, 2013). A parametrized functional form for a monotonic relationship between the H I and halo mass is assumed to obtain the HIHM relation. The best-fitting values of the parameters that fit the observed H I-mass function from radio data are then obtained. This approach of modelling the HIHM relation at $z = 0$ from the radio data at low redshifts has been followed previously by Papastergis et al. (2013). Our abundance matched HIHM agrees with that derived by these authors.

We further explore how well the abundance matching approach at $z = 0$ can be constrained by fitting to the high-redshift data. We extend the low-redshift determination of the HIHM relation by postulating that the evolution of the HIHM relation is similar to the SHM relation. We parametrize this evolution analogously to the evolution of the SHM relation by Moster et al. (2013). The physical motivation for the parametrization is that the H I-follows-stars functional form works well at low redshifts, which is in turn a consequence of the fact that the underlying mass/luminosity functions can be described by the Schechter form. Observational measurements of the H I-mass function are not yet available at these redshifts. Hence, we use measurements of the H I column density distribution function and the H I clustering from UV/optical observations of quasar absorption spectra. We assume that high column density systems (DLAs; $N_{\rm H\,I} > 10^{20.3}$ cm^{-2}) probe systems are high-redshift analogues of H I in galaxies detected in radio surveys at low redshifts (Zwaan et al. 2005b).

Our procedure allows a modelling of low- and high-redshift measurements of the H I content of galaxies to obtain the evolution of the HIHM relation from $z = 0$ to 2.3 with the associated uncertainty. This technique is complementary to the forward modelling approach that aims to characterize H I using a halo model framework similar to that of the underlying dark matter (Padmanabhan & Refregier 2017). However, this work represents a first attempt to characterize the HIHM relation empirically, directly from the data. Due to the sparse nature of the high-redshift data at present, there is considerable scatter in the high-redshift HIHM relation. As a

result, other apparently dissimilar models from the literature are also consistent with the data and the allowed range of this work. The scatter in the HIHM relation at higher redshifts can be reduced with tighter constraints on the H I-mass functions from upcoming and future radio surveys.

Our results provide a useful benchmark to calibrate the H I physics in hydrodynamical simulations, especially at low redshifts where correct treatment of star formation and feedback as well as cooling and formation of molecular hydrogen are critical. They also provide an estimate of the uncertainty in the HIHM relation coming from the high-redshift data and motivate further work towards possibly tighter constraints on the HIHM relation.

ACKNOWLEDGEMENTS

We thank Alireza Rahmati, Alexandre Refregier and Sergey Koposov for useful discussions, and Robert Crain for kindly providing the data from the EAGLE simulations. This work has made use of the VizieR catalogue access tool, CDS, Strasbourg, France. The original description of the VizieR service was published in the A&AS 143, 23. HP's research is supported by the Tomalla Foundation. GK gratefully acknowledges support from the ERC Advanced Grant 320596 'The Emergence of Structure During the Epoch of Reionization'.

REFERENCES

Abazajian K. N. et al., 2009, ApJS, 182, 543
Akeret J., Seehars S., Amara A., Refregier A., Csillaghy A., 2013, Astron. Comput., 2, 27
Bagla J. S., Khandai N., Datta K. K., 2010, MNRAS, 407, 567
Bahé Y. M. et al., 2016, MNRAS, 456, 1115
Baldry I. K., Glazebrook K., Driver S. P., 2008, MNRAS, 388, 945
Bandura K. et al., 2014, in Stepp L. M., Gilmozzi R., Hall H. J., eds, Proc. SPIE Conf. Ser. Vol. 9145, Ground-based and Airborne Telescopes V. SPIE, Bellingham, p. 914522
Barkana R., 2016, Phys. Rep., 645, 1
Barnes L. A., Haehnelt M. G., 2009, MNRAS, 397, 511
Barnes L. A., Haehnelt M. G., 2010, MNRAS, 403, 870
Barnes L. A., Haehnelt M. G., 2014, MNRAS, 440, 2313
Behroozi P. S., Conroy C., Wechsler R. H., 2010, ApJ, 717, 379
Berry M., Somerville R. S., Haas M. R., Gawiser E., Maller A., Popping G., Trager S. C., 2014, MNRAS, 441, 939
Bird S., Vogelsberger M., Haehnelt M., Sijacki D., Genel S., Torrey P., Springel V., Hernquist L., 2014, MNRAS, 445, 2313
Bird S., Haehnelt M., Neeleman M., Genel S., Vogelsberger M., Hernquist L., 2015, MNRAS, 447, 1834
Blanton M. R., Moustakas J., 2009, ARA&A, 47, 159
Bouché N. et al., 2010, ApJ, 718, 1001
Boylan-Kolchin M., Springel V., White S. D. M., Jenkins A., Lemson G., 2009, MNRAS, 398, 1150
Catinella B. et al., 2010, MNRAS, 403, 683
Catinella B. et al., 2012, A&A, 544, A65
Catinella B. et al., 2013, MNRAS, 436, 34
Cen R., 2012, ApJ, 748, 121
Chang T.-C., Pen U.-L., Bandura K., Peterson J. B., 2010, Nature, 466, 463
Conroy C., Wechsler R. H., Kravtsov A. V., 2006, ApJ, 647, 201
Crain R. A. et al., 2015, MNRAS, 450, 1937
Crain R. A. et al., 2017, MNRAS, 464, 4204
Davé R., Katz N., Oppenheimer B. D., Kollmeier J. A., Weinberg D. H., 2013, MNRAS, 434, 2645
Delhaize J., Meyer M. J., Staveley-Smith L., Boyle B. J., 2013, MNRAS, 433, 1398
Duffy A. R., Kay S. T., Battye R. A., Booth C. M., Dalla Vecchia C., Schaye J., 2012, MNRAS, 420, 2799
Evoli C., Salucci P., Lapi A., Danese L., 2011, ApJ, 743, 45
Fabello S., Kauffmann G., Catinella B., Li C., Giovanelli R., Haynes M. P., 2012, MNRAS, 427, 2841
Font-Ribera A. et al., 2012, J. Cosmol. Astropart. Phys., 11, 59
Fu J., Guo Q., Kauffmann G., Krumholz M. R., 2010, MNRAS, 409, 515
Fu J., Kauffmann G., Li C., Guo Q., 2012, MNRAS, 424, 2701
Gardner J. P., Katz N., Hernquist L., Weinberg D. H., 1997, ApJ, 484, 31
Giovanelli R. et al., 2005, AJ, 130, 2598
Gong Y., Chen X., Silva M., Cooray A., Santos M. G., 2011, ApJ, 740, L20
Guha Sarkar T., Mitra S., Majumdar S., Choudhury T. R., 2012, MNRAS, 421, 3570
Guo Q., White S., Li C., Boylan-Kolchin M., 2010, MNRAS, 404, 1111
Haehnelt M. G., Rauch M., Steinmetz M., 1996, MNRAS, 283, 1055
Haehnelt M. G., Steinmetz M., Rauch M., 1998, ApJ, 495, 647
Hong S., Katz N., Davé R., Fardal M., Kereš D., Oppenheimer B. D., 2010, preprint (arXiv:1008.4242)
Jonas J. L., 2009, Proc. IEEE, 97, 1522
Kauffmann G., Huang M.-L., Moran S., Heckman T. M., 2015, MNRAS, 451, 878
Kim H.-S., Power C., Baugh C. M., Wyithe J. S. B., Lacey C. G., Lagos C. D. P., Frenk C. S., 2013, MNRAS, 428, 3366
Kim H.-S., Wyithe J. S. B., Baugh C. M., Lagos C. d. P., Power C., Park J., 2017, MNRAS, 465, 111
Krumholz M. R., Dekel A., 2012, ApJ, 753, 16
Kulkarni G., Rollinde E., Hennawi J. F., Vangioni E., 2013, ApJ, 772, 93
Lagos C. D. P., Baugh C. M., Lacey C. G., Benson A. J., Kim H.-S., Power C., 2011, MNRAS, 418, 1649
Lagos C. d. P., Davis T. A., Lacey C. G., Zwaan M. A., Baugh C. M., Gonzalez-Perez V., Padilla N. D., 2014, MNRAS, 443, 1002
Lah P. et al., 2007, MNRAS, 376, 1357
Lah P. et al., 2009, MNRAS, 399, 1447
Lanzetta K. M., Wolfe A. M., Turnshek D. A., Lu L., McMahon R. G., Hazard C., 1991, ApJS, 77, 1
Leroy A. K., Walter F., Brinks E., Bigiel F., de Blok W. J. G., Madore B., Thornley M. D., 2008, AJ, 136, 2782
Leroy A. K. et al., 2009, AJ, 137, 4670
Li C., White S. D. M., 2009, MNRAS, 398, 2177
Li C., Kauffmann G., Fu J., Wang J., Catinella B., Fabello S., Schiminovich D., Zhang W., 2012, MNRAS, 424, 1471
Macciò A. V., Dutton A. A., van den Bosch F. C., Moore B., Potter D., Stadel J., 2007, MNRAS, 378, 55
Maller A. H., Bullock J. S., 2004, MNRAS, 355, 694
Maller A. H., Prochaska J. X., Somerville R. S., Primack J. R., 2001, MNRAS, 326, 1475
Marín F. A., Gnedin N. Y., Seo H.-J., Vallinotto A., 2010, ApJ, 718, 972
Martin A. M., Papastergis E., Giovanelli R., Haynes M. P., Springob C. M., Stierwalt S., 2010, ApJ, 723, 1359
Martindale H., Thomas P. A., Henriques B. M., Loveday J., 2016, preprint (arXiv:1606.08440)
Masui K. W. et al., 2013, ApJ, 763, L20
Meyer M. J. et al., 2004, MNRAS, 350, 1195
Moster B. P., Somerville R. S., Maulbetsch C., van den Bosch F. C., Macciò A. V., Naab T., Oser L., 2010, ApJ, 710, 903
Moster B. P., Naab T., White S. D. M., 2013, MNRAS, 428, 3121
Nagamine K., Wolfe A. M., Hernquist L., Springel V., 2007, ApJ, 660, 945
Navarro J. F., Frenk C. S., White S. D. M., 1996, ApJ, 462, 563
Noterdaeme P. et al., 2012, A&A, 547, L1
Obreschkow D., Croton D., De Lucia G., Khochfar S., Rawlings S., 2009, ApJ, 698, 1467
Padmanabhan H., Refregier A., 2017, MNRAS, 464, 4008
Padmanabhan H., Choudhury T. R., Refregier A., 2015, MNRAS, 447, 3745
Padmanabhan H., Choudhury T. R., Refregier A., 2016, MNRAS, 458, 781
Papastergis E., Cattaneo A., Huang S., Giovanelli R., Haynes M. P., 2012, ApJ, 759, 138
Papastergis E., Giovanelli R., Haynes M. P., Rodríguez-Puebla A., Jones M. G., 2013, ApJ, 776, 43
Pérez-González P. G. et al., 2008, ApJ, 675, 234
Pontzen A. et al., 2008, MNRAS, 390, 1349

Popping A., Davé R., Braun R., Oppenheimer B. D., 2009, A&A, 504, 15
Popping G., Somerville R. S., Trager S. C., 2014, MNRAS, 442, 2398
Popping G., Behroozi P. S., Peeples M. S., 2015, MNRAS, 449, 477
Prochaska J. X., Wolfe A. M., 1997, ApJ, 487, 73
Prochaska J. X., Wolfe A. M., 2009, ApJ, 696, 1543
Rahmati A., Schaye J., 2014, MNRAS, 438, 529
Rahmati A., Pawlik A. H., Raicevic M., Schaye J., 2013, MNRAS, 430, 2427
Rao S., Briggs F., 1993, ApJ, 419, 515
Rao S. M., Turnshek D. A., Nestor D. B., 2006, ApJ, 636, 610
Rhee J., Zwaan M. A., Briggs F. H., Chengalur J. N., Lah P., Oosterloo T., Hulst T. v. d., 2013, MNRAS, 435, 2693
Rodríguez-Puebla A., Avila-Reese V., Firmani C., Colín P., 2011, Rev. Mex. Astron. Astrofis., 47, 235
Saintonge A. et al., 2011a, MNRAS, 415, 32
Saintonge A. et al., 2011b, MNRAS, 415, 61
Santini P. et al., 2012, A&A, 538, A33
Santos M. et al., 2015, Proc. Sci., Cosmology from a SKA H I intensity mapping survey. SISSA, Trieste, PoS(AASKA14)19
Sarkar D., Bharadwaj S., Anathpindika S., 2016, MNRAS, 460, 4310
Schaye J. et al., 2015, MNRAS, 446, 521
Scoccimarro R., Sheth R. K., Hui L., Jain B., 2001, ApJ, 546, 20
Shankar F., Lapi A., Salucci P., De Zotti G., Danese L., 2006, ApJ, 643, 14
Sheth R. K., Tormen G., 2002, MNRAS, 329, 61
Somerville R. S., Davé R., 2015, ARA&A, 53, 51
Somerville R. S., Popping G., Trager S. C., 2015, MNRAS, 453, 4337
Springel V. et al., 2005, Nature, 435, 629
Switzer E. R. et al., 2013, MNRAS, 434, L46
Tescari E., Viel M., Tornatore L., Borgani S., 2009, MNRAS, 397, 411
Vale A., Ostriker J. P., 2004, MNRAS, 353, 189
Vale A., Ostriker J. P., 2006, MNRAS, 371, 1173
van de Voort F., Schaye J., Booth C. M., Haas M. R., Dalla Vecchia C., 2011, MNRAS, 414, 2458
van der Hulst J. M., van Albada T. S., Sancisi R., 2001, in Hibbard J. E., Rupen M., van Gorkom J. H., eds, ASP Conf. Ser. Vol. 240, Gas and Galaxy Evolution. Astron. Soc. Pac., San Francisco, p. 451
Walter F., Brinks E., de Blok W. J. G., Bigiel F., Kennicutt R. C., Jr, Thornley M. D., Leroy A., 2008, AJ, 136, 2563
Wolfe A. M., Turnshek D. A., Smith H. E., Cohen R. D., 1986, ApJS, 61, 249
Wyithe J. S. B., Brown M. J. I., 2010, MNRAS, 404, 876
York D. G. et al., 2000, AJ, 120, 1579
Zafar T., Péroux C., Popping A., Milliard B., Deharveng J.-M., Frank S., 2013, A&A, 556, A141
Zhang W., Li C., Kauffmann G., Xiao T., 2013, MNRAS, 429, 2191
Zwaan M. A., Meyer M. J., Staveley-Smith L., Webster R. L., 2005a, MNRAS, 359, L30
Zwaan M. A., van der Hulst J. M., Briggs F. H., Verheijen M. A. W., Ryan-Weber E. V., 2005b, MNRAS, 364, 1467

This paper has been typeset from a TEX/LATEX file prepared by the author.